International Journal of Greenhouse Gas Control 129 (2023) 103984

Contents lists available at ScienceDirect

International Journal of Greenhouse Gas Control

journal homepage: www.elsevier.com/locate/ijggc

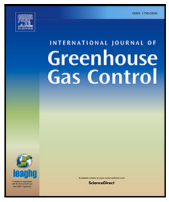

Viscosification of CO_2 to improve subsurface storage — A modeling study

Joachim Moortgat [a,b,*], Abbas Firoozabadi [c]

[a] School of Earth Sciences, The Ohio State University, Columbus, 43210, OH, USA
[b] Byrd Polar and Climate Research Center, The Ohio State University, Columbus, 43210, OH, USA
[c] Rice University, Chemical and Biomolecular Engineering Department, Houston, 77005, TX, USA

ARTICLE INFO

Keywords:
CO_2 storage
CO_2 viscosification
Reservoir simulation

ABSTRACT

In this work, we numerically investigate the potential benefits of a recently proposed functional molecule that can both significantly increase the viscosity of CO_2 and reduce the residual water saturation in the context of CO_2 storage in subsurface aquifers. We model different degrees of CO_2 viscosification in field-scale formations at both shallow and greater depths, consider a range of permeabilities from 100 md to 2,000 md, and both homogeneous and highly heterogeneous formations. To quantify the impacts of CO_2 viscosification, we track multiple domain-integrated quantitative measures such as CO_2 tip velocity and dispersion widths. In all scenarios, we find that CO_2 viscosification increases the total amount of CO_2 retained but the degree of improvement varies. Moreover, the fraction of solubility trapping versus structural trapping is highest for neat CO_2. These modeling results can inform stakeholders in CO_2 viscosification technology for future large-scale CO_2 storage projects.

1. Introduction

Increases in CO_2 and other greenhouse gases in the atmosphere have risen dramatically in the past 150 years, posing significant climate concerns. Efforts to reduce anthropogenic CO_2 emissions include storing it in subsurface aquifers. The Sleipner aquifer in the North Sea has shown promising results in a large-scale CO_2 storage project, with minimal pressure buildup after continuous injection for over 25 years. Saline aquifers, found worldwide and spanning long distances, offer greater storage potential than depleted oil and gas fields due to their extensive volume (Firoozabadi and Myint, 2010). These formations can have high permeability and porosity, facilitating high injection rates and ample pore space for storage.

CO_2 in the subsurface exists in a supercritical state, displaying gas-like viscosity and liquid-like density. While its density can surpass that of oil, it remains lower than the density of brine. As a result, CO_2 tends to rise quickly, accumulate beneath the cap-rock, and spread widely. The cap-rock acts as an effective seal if it extends to where CO_2 spreads; however, well penetration or fractures in the cap-rock can create pathways for CO_2 leakage.

Following injection, CO_2 can be retained in four categories (Ide et al., 2007): (1) highly mobile free supercritical CO_2 structurally trapped below the cap rock, (2) residual trapping in pores due to capillary effects, (3) solubility trapping of CO_2 dissolved in the aqueous phase, and (4) mineral trapping when CO_2 reacts with the rock formation. Structural trapping can be improved by both controlling mobility and by reducing residual brine saturations, both of which retard lateral migration. Mobility control can be achieved by reducing CO_2 relative permeability or by direct viscosification.

Three potential technologies for CO_2 mobility control are: (1) alternate injection of CO_2 and brine, (2) CO_2-foam injection, and (3) the use of a functional molecule to directly viscosify CO_2. The first two options have been extensively studied through lab and field-scale experiments, as well as numerical modeling. The third option has only recently been investigated in lab experiments (Kar and Firoozabadi, 2022; Afra et al., 2023), and this study aims to analyze the potential benefits of this novel technology in field-scale applications using detailed reservoir simulations.

To provide context, we first present a brief overview of earlier lab- and field-scale studies of the first two options for mobility control.

Reports on CO_2-foam in brine-saturated rocks are somewhat limited. A study by Adebayo (2018) examined CO_2-foam in low and high permeability rocks using a low concentration of a foaming agent dissolved in brine. Rocks were initially saturated with surfactant solutions before injecting alternating slugs of CO_2 and surfactant. Subsequent analysis of foam stability found that CO_2 saturations vanished within 80 mins and the authors concluded that CO_2-foam stabilizers would be required. Another study by Føyen et al. (2020) reported on CO_2-foam core flooding experiments using different commercial foaming agents and a 1.15 m long vertical sandstone core. High apparent CO_2 viscosities were

* Corresponding author.
E-mail address: moortgat.1@osu.edu (J. Moortgat).

https://doi.org/10.1016/j.ijggc.2023.103984
Received 26 November 2022; Received in revised form 13 July 2023; Accepted 6 September 2023

observed together with a decrease in residual brine saturation (S_{wr}), which is an important finding.

Large-scale simulations of CO_2-foam have been carried out by different research groups. Vitoonkijvanich et al. (2015) used an in-house streamline as well as a commercial simulator to examine both simultaneous and alternating surfactant-CO_2 injection at different fractional flows with foam models from Hirasaki and Lawson (1985) and Rossen et al. (1999). A quarter-five-spot 3D domain of about $366 \times 670 \times 52$ m^3, discretized by $20 \times 55 \times 17$ grid cells, was modeled with heterogeneous permeability varying from 0.01 md to 700 md with most of the domain in the 10 md range. Capillary pressures were neglected and the residual brine saturation was assumed to be 20%. The authors include strong- and weak-foam in the course of CO_2-assisted foam injection. Their results show that CO_2 sweep efficiency is poor for neat CO_2 injection and higher for brine-coinjection with CO_2, and much higher in surfactant co-injection with CO_2. However, CO_2 breakthrough is fast in all cases. Key findings from their study were that: (1) the fraction of pore volume filled with CO_2 at abandonment in brine- and foam-assisted CO_2 storage are around 18% and 23%, respectively, and (2) the amount of water needed per pore volume of CO_2 stored was about 5–60 m^3/m^3 for CO_2-foam. Vitoonkijvanich et al. (2015) state that foam degradation before or close to brine injection may provide the optimum sequestration strategy. Injection of hot water to chase brine can help the degradation and improve the sweep. The authors do not provide information on pressure build-up in the injection well.

Field-scale modeling with a commercial simulator and an analytical model by Izadi and Kam (2020) investigated the effects of injection rate (or pressure) and foam quality, conversion from strong foam to weak foam, and gravity segregation. Their work shows that the foam propagation distance increases with higher injection pressures and with a decrease in foam quality down to a certain threshold. They assume a homogeneous reservoir with open boundaries and incompressible brine. Depending on the foam quality, the injection pressure at near steady state reached 193 bar (70% foam quality) and 152 bar (90% quality), up from the initial 107 bar reservoir pressure.

Lyu et al. (2021) also performed a large-scale investigation of foam-assisted CO_2 storage in saline aquifers with an in-house simulator, accounting for several mechanisms related to foam flow. They modeled a 5° section of a 400-m radius, 30-m thick 3D reservoir with 100 md permeability. In one year, about 2.3% PV of CO_2 was injected at a constant rate from the center. To avoid complexities from water injection, the surfactant was placed uniformly in the formation. The phase-behavior from dissolution of CO_2 in brine was modeled with an activity coefficient approach, with the Peng–Robinson equation of state (Peng and Robinson, 1976) describing the CO_2 phase. Their simulation results show that for neat CO_2 injection, there is quick gravitational segregation of CO_2 to the top, spreading about 350 m in a year. For CO_2-foam, the sweep efficiency was significantly improved with CO_2 only spreading 125 m during the same period. For neat CO_2, pressures increased less than 4 bar from the initial 90 bar formation pressure, while the pressure increased to 125 bar for CO_2-foam.

Further challenges related to CO_2-foam for carbon sequestration are reviewed in a recent work by Rossen et al. (2022). There are two key issues in foam-assisted storage of CO_2 in saline aquifers: (1) injectivity-loss because of the high viscosity and co-injection of brine, and (2) injection of large volumes of water. These are the motivation to find alternative approaches that can directly viscosify CO_2 without the need for co-injection of water.

Kar and Firoozabadi (2022) recently reported on successful direct CO_2 viscosification using an oligomer of 1-decene. At a concentration of 1.5 wt% in CO_2, they observe a fivefold increase in viscosity. Unique and desirable features of the oligomer are: low adsorption to rock, low solubility in brine, and no effect of salt concentration in brine on the performance of the molecule. Afra et al. (2023) conducted experiments on brine production from brine-saturated Berea cores with neat versus viscosified CO_2 injection at subsurface temperatures and pressures. Experimental results show a 200%–300% delay in CO_2 breakthrough, due to the reduced mobility, and a 30% reduction in S_{wr}. Kar et al. (2022) argue that the S_{wr}-reduction is likely due to interfacial viscoelasticity rather than interfacial tension effects.

The purpose of this work is to provide preliminary insights into how the viscosification technique proposed by Kar and Firoozabadi (2022) and Afra et al. (2023) might perform in near-future field-scale applications. To this end, we present simulation results for different degrees of viscosification and a wide range of reservoir conditions, such as shallow and deep formation temperatures and pressures, different permeability ranges, and homogeneous versus heterogeneous rock properties. For each scenario, we provide 3D illustrative simulation results of the CO_2 spreading behavior over time, as well as nine different domain-integrated metrics that quantitatively measure the efficiency of the CO_2 viscosification under different conditions.

2. Methods

2.1. Simulator description

The simulations presented in this work are carried out with our in-house reservoir simulator, *Osures*. *Osures* is based on higher-order mixed finite element (MFE) methods with low grid sensitivity and numerical dispersion (Moortgat and Firoozabadi, 2016; Moortgat et al., 2016; Moortgat, 2017), which are particularly well suited for strongly heterogeneous, layered, and fractured formations and allow for tensor permeabilities and unstructured grids (Moortgat and Firoozabadi, 2013b,c; Moortgat et al., 2018; Moortgat and Firoozabadi, 2017). These FE methods are also strictly mass-conserving at the grid-cell level. *Osures* incorporates rigorous thermodynamic phase-stability and phase-split computations that guarantee minimum Gibbs free energy and equality of all species' fugacities in all phases. These computations are based on an equation of state (EOS). Popular EOS like Peng–Robinson and Soave–Redlich–Kwong can work well for non-polar molecules, such as hydrocarbons, but cannot account for self-association and cross-associate when there are molecules with polar (or polar-induced) moments. We have developed a Cubic-Plus-Association EOS that can more accurately model the phase behavior of mixtures of polar water, CO_2, methane and other components (Li and Firoozabadi, 2009; Moortgat, 2018; Nasrabadi et al., 2016; Moortgat et al., 2011).

Fickian diffusion can play an important role in CO_2 sequestration because it (1) drives the dissolution of CO_2 into brine, (2) determines the critical onset time and wavelength of gravitational instabilities (Soltanian et al., 2016b), and (3) facilitates cross-flow between layers or fractures with different permeabilities. Our diffusion model accounts for the different species compositions in each phase (Hoteit and Firoozabadi, 2009; Moortgat and Firoozabadi, 2013a). For a two-component water-CO_2 mixture, a simplified diffusion model with a single coefficient in each phase is sufficient. Note, however, that unlike many works, we also allow H_2O to evaporate from the brine into the super-critical CO_2-rich phase, so both phase have two varying species compositions and associated diffusion.

Osures has been validated extensively for CO_2 injection problems, both against experimental data (Moortgat et al., 2010; Moortgat and Firoozabadi, 2013a, 2017; Moortgat et al., 2013) and for field-scale CO_2 sequestration projects (Soltanian et al., 2016a, 2018a,b). To model the benefits of viscosified CO_2, we simply multiply the measured viscosity of neat CO_2 at a given temperature and pressure by a certain user-defined factor. This approach is based on the experimental observations that the viscosification is thermodynamically stable and does not affect the brine phase.

Relative permeabilities for water and CO_2 are modeled by standard Brooks–Corey relationships, the parameters of which are provided in each example.

2.2. Quantitative measures of CO_2 migration

To quantitatively analyze the CO_2 flow dynamics for different levels of viscosification, we track the following global measures:

1. CO_2 plume tip location, defined as the largest radius for which a grid cell has an overall molar fraction of ≥5 mole %.
2. Tip velocity, obtained by taking the finite different derivative of tip locations versus time.
3. The center-of-mole (COM) coordinates z_{ave} and R_{ave} (with radius $R \approx x$ for the 5° wedge modeled in the examples). These are defined as the first spatial moments of the CO_2 molar density $C = cz_{\text{CO2}}$ with c the total molar density and z_{CO2} the molar fraction of CO_2 in the two-phase mixture. In discrete form, we have (Amooie et al., 2018, 2017):

$$z_{\text{ave}} = \frac{\langle C \times z \rangle}{\langle C \rangle}, \tag{1}$$

$$R_{\text{ave}} = \frac{\langle C \times R \rangle}{\langle C \rangle}, \tag{2}$$

$$\langle (\cdot) \rangle = \frac{\sum_{k\in\Omega} (\cdot)\phi_k V_k}{\sum_{k\in\Omega} \phi_k V_k}, \tag{3}$$

with ϕ_k and V_k the porosity and volume of grid cell k in the domain Ω.

4. The dispersion widths σ_z and σ_R, which measure the degree of spreading relative to the COM coordinates, defined in terms of the second spatial moments of the total CO_2 molar density as:

$$\sigma_z = \sqrt{\frac{\langle C \times z^2 \rangle}{\langle C \rangle} - z_{\text{ave}}}, \tag{4}$$

$$\sigma_{\text{R}} = \sqrt{\frac{\langle C \times R^2 \rangle}{\langle C \rangle} - R_{\text{ave}}}. \tag{5}$$

5. The total fraction (or percentage) of CO_2 throughout the domain that is dissolved in the aqueous phase, i.e., the fraction of solubility trapping versus structural trapping of free super-critical CO_2. Denoting water and gas saturations as S_w and S_g; molar densities of water and gas as c_w and c_g; molar fractions of CO_2 in the water and gas phases as $x_{\text{CO2},g}$ and $x_{\text{CO2},w}$; and using short-hand notation $C_w = c_w x_{\text{CO2},w}$ and $C_g = c_g x_{\text{CO2},g}$, we define:

$$\text{CO}_{2,w} = \frac{\sum_{k\in\Omega} (S_w C_w)\phi_k V_k}{\sum_{k\in\Omega} C\phi_k V_k} \tag{6}$$

$$= \frac{\sum_{k\in\Omega} (S_w C_w)\phi_k V_k}{\sum_{k\in\Omega} (S_w C_w + (1-S_w)C_g)\phi_k V_k}. \tag{7}$$

Note that for a two-component mixture of CO_2 and water, C_w and C_g do not depend on the overall composition z_{CO2} but only on pressure (under isothermal conditions). For modest pressure gradients, C_g/C_w is nearly constant and the degree of solubility trapping is primarily determined by the saturation distribution throughout the domain, which in turn is a result of the gas and water flow rates as a function of mobility ratios.

6. Storage efficiency. Because we assume a constant CO_2 injection rate in all simulations, the total amount of CO_2 stored in the subsurface at any time is known a priori. As an efficiency metric, we instead track the fraction of injected CO_2 that remains within the modeled domain, e.g., within a 400 m radius around the injection well.

3. Simulation set-ups

3.1. Domain geometries, initial and boundary conditions

Lyu et al. (2021) modeled foam-assisted storage of CO_2 in saline aquifers as a method to reduce CO_2 mobility. Here, we model a similar problem set-up to offer a comparison to thermodynamically stable CO_2 viscosification by functional molecules. Specifically, we model the same 3D domain with a thickness of 30 m and a 400 m radius around a single vertical perforated well. For computational efficiency, we take advantage of the axial symmetry and only model a 5° segment of the cylindrical geometry. We construct a fine logically Cartesian grid of $400 \times 16 \times 60 = 384{,}000$ non-orthogonal hexahedra that are refined near the well as illustrated in Fig. 1. The finest grid cells near the well are 1 m × 10 cm × 50 cm (i.e., significantly higher resolution than in Lyu et al. (2021)).

As in Lyu et al. (2021), we consider an initial pressure at the bottom of 90 bar, and an (isothermal) temperature is 323 °K. Temperature and pressure conditions representative of deeper saline aquifers will be considered as well (specifically, 373 °K and 241 bar).

CO_2 is injected from the full 30 m vertical extent of the formation at a rate of 6% pore volume (PV) per year (or ∼10 m^3/day, which is 2.5 times higher than in Lyu et al. (2021)). The right-most boundary is open to flow (kept at the initial hydrostatic vertical pressure distribution) and all other boundaries are closed.

3.2. Rock properties

We assume a uniform porosity of 30% and model a range of rock permeability conditions. We start with the same relatively low uniform permeability of 100 md as in Lyu et al. (2021), but also consider layered systems with a tenfold permeability contrast (e.g., 10 md and 100 md layers, or 100 md and 1000 md layers), an intermediate uniform permeability of 500 md, and high permeabilities of 2000 md in which gravitational segregation and fingering instabilities are far more pronounced. High permeabilities are preferred for CO_2 storage because of high injectivity and effective convective mixing of dissolved CO_2 as a result of gravitational instabilities. However, the adverse mobility ratio of injected CO_2 versus formation brine can lead to fast lateral spreading of CO_2 in the top of the formation and/or through high permeability pathways in heterogeneous formations. Therefore, this is an interesting set of conditions to study the advantageous effects of CO_2 viscosification.

In contrast to these mostly uniform aquifers, we also model the effects of CO_2 viscosification for a highly heterogeneous fluvial depositional environment, specifically, as encountered in the Cranfield large volume CO_2 storage pilot project (Hovorka et al., 2011; Hosseini et al., 2013; Soltanian et al., 2016a)

3.3. Relative permeabilities

For the two-phase CO_2-brine flow process we assume the same Brooks–Corey relative permeabilities as in Lyu et al. (2021) with powers of 4 and 2 and end-points of 1 and 0.4 for brine and supercritical CO_2, respectively. Lyu et al. (2021) use an unusually low residual water saturation of $S_{wr} = 20\%$ in neat CO_2 injection. For some of our simulations we consider a higher $S_{wr} = 40\%$ and also model the effect of residual water reduction by the functional molecules co-injected with CO_2.

For the Cranfield problem, we use the same relative permeability parameters as in Soltanian et al. (2016a) and earlier studies cited therein, which have similar powers (4.2 and 2.6 for water and gas, respectively).

While using the aforementioned parameters in this work, we note that (1) there are unresolved challenges in measuring relative permeabilities from core flood experiments, (2) CO_2 may alter the rock wettability, and (3) we expect relative permeabilities to vary between different facies in heterogeneous formations. As such, these parameters are one of the largest uncertainties in modeling CO_2 storage in, especially heterogeneous, subsurface formations.

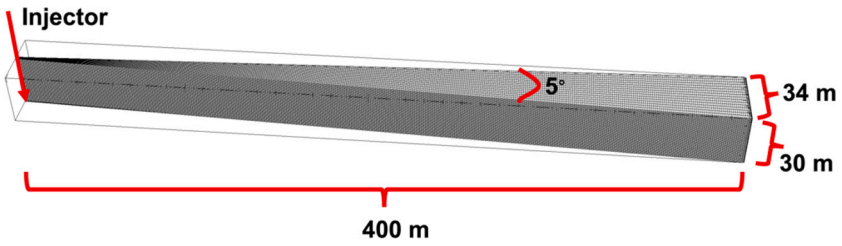

Fig. 1. Computational grid of 384,000 hexahedral elements, geometric dimensions, and location of injection well.

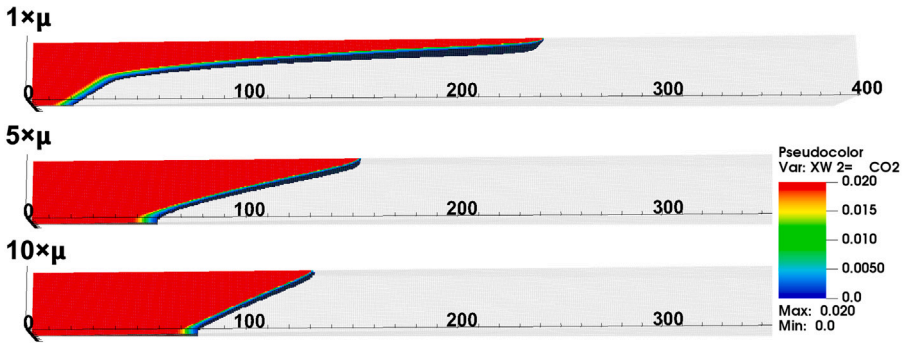

Fig. 2. Case 1: $x_{CO2,w}$ after 1 year injection at 6% PV/yr of neat CO_2 ($1\times\mu$), 5× viscosified CO_2 ($5\times\mu$), and 10× viscosified CO_2 ($10\times\mu$) for a formation with uniform permeability of $K = 100$ md. All following figures for this domain will use the same color scale and a cut-off threshold of 0.1 mole % dissolved CO_2.

3.4. Phase behavior

The phase behavior of the CO_2-brine system is modeled by the Cubic-Plus-Association (CPA) Equation-of-State (EOS) (Moortgat, 2018; Nasrabadi et al., 2016; Moortgat et al., 2011). As stated, our CPA-EOS based phase-split computations accurately account not only for the CO_2 solubility in the aqueous phase, but also the water evaporation into the CO_2-rich phase. The latter means that water saturations can be reduced to below the residual saturations due to evaporation, particularly near the injection well. At the permeabilities and reservoir pressures considered in this work, capillary effects are neglected.

As for the critical parameter of this study, the CO_2 viscosity (denoted as μ): for the different temperature and pressure conditions (corresponding to different formation depths) and rock properties, we compare simulations of neat CO_2 injection to simulations in which the CO_2 is viscosified by factors of 5, 10, and/or 15. We also model a more economically attractive scenario in which viscosified CO_2 is only injected for the first year, followed by (cheaper) neat CO_2 injection. Finally, in a few simulations we also consider the reduction in residual water saturation associated with viscosified CO_2 (Ding et al., 2023; Afra et al., 2023).

4. Results

This section presents the results from a wide range of simulations for different formation properties and CO_2 injection strategies, e.g. with and without viscosification treatments. For each case, we show the molar fraction of *dissolved* CO_2, $x_{CO2,w}$, throughout the domain and over time, which most clearly visualizes both the sweep of free supercritical CO_2 (leaving behind fully saturated residual water) as well as gravitational fingering caused by dissolved CO_2 below the free-CO_2-water interface. Plume tip location and velocity, horizontal and vertical COM and dispersion widths, overall fraction of dissolved CO_2, and pressure response are provided in the Supplemental Information and interpreted in the Discussion.

4.1. Shallow formation

At the initial temperature (323 °K) and pressure (90 bar) of this formation, the neat CO_2 and aqueous viscosities are 0.025 cp and 0.544 cp, respectively, so the adverse viscosity ratio is a factor 22. The mass densities are 296 kg/m^3 for CO_2 and 1003 kg/m^3 for brine. At the initial pressure, the CO_2 solubility is 2 mole %, which increases the aqueous density by 1.2%.

Case 1: Low permeability of 100 md. The first simulation is for a relatively low permeability of 100 md, as in Lyu et al. (2021) (and using all the same parameters, including $S_{wr} = 20\%$). Fig. 2 compares the CO_2 sweep after one year of injection at 6% pore volume (PV) per year for different degrees of viscosification. Additional snapshots after 2, 3, and 6 years are provided in Figures SI1–3, and the global metrics are summarized in Figure SI4.

Case 2: Layered formation. It is sometimes assumed that gravitational segregation and fingering instabilities are less pronounced in layered porous media, which have a lower effective vertical permeability. We model two simple set-ups with a ten-fold contrast in permeabilities between the top and bottom halves of the formation. Fig. 3 shows the CO_2 flow paths when the permeabilities are 100 md in the top and 1000 md in the bottom (Case 2a), and Fig. 4 has 100 md in the bottom and 10 md in the top (Case 2b). The corresponding global metrics are provided in Figures SI5 and SI6.

Case 3: High permeability of 2000 md. High permeability saline aquifers are attractive for CO_2 storage, because they have the highest injectivity and fastest gravito-convective mixing of dissolved CO_2 (solubility trapping). However, they are also the most prone to significant gravitational override and thus poor sweep efficiency. To investigate the beneficial impacts of CO_2 viscosification on storage in high permeability formations, we consider a uniform $K = 2000$ md. As an additional challenge for CO_2 storage, we assume a higher residual water saturation of $S_{wr} = 40\%$ to neat CO_2. Moreover, we assume that the viscosified CO_2 also reduces S_{wr} by 25%, i.e. to $S_{wr} = 30\%$, similar to the experimental findings in Kar and Firoozabadi (2022).

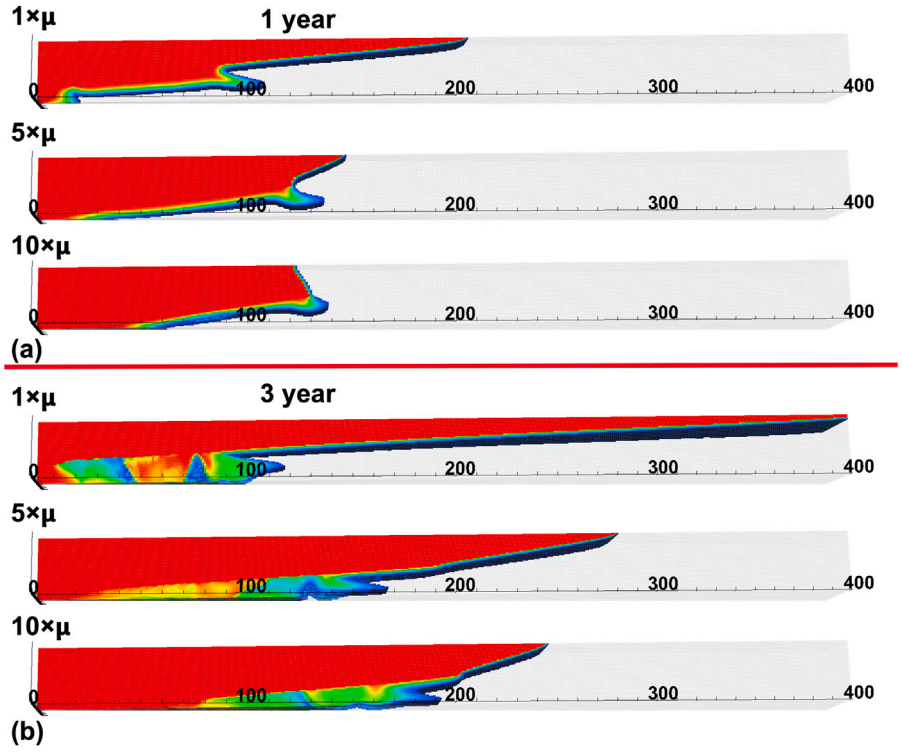

Fig. 3. Case 2a: $x_{CO2,w}$ after 1 (a) and 3 (b) years of injection for a layered formation with permeability of $K = 100$ md for $z \geq 15$ m and $K = 1000$ md for $z < 15$ m.

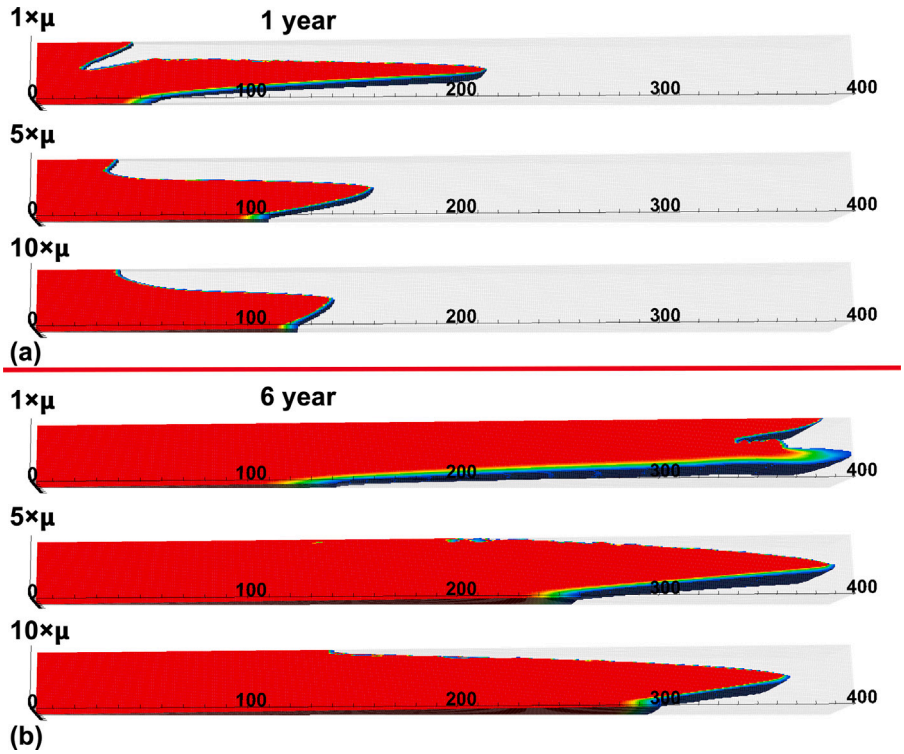

Fig. 4. Case 2b: $x_{CO2,w}$ after 1 (a) and 3 (b) years of injection for a layered formation with permeability of $K = 10$ md for $z \geq 15$ m and $K = 100$ md for $z < 15$ m.

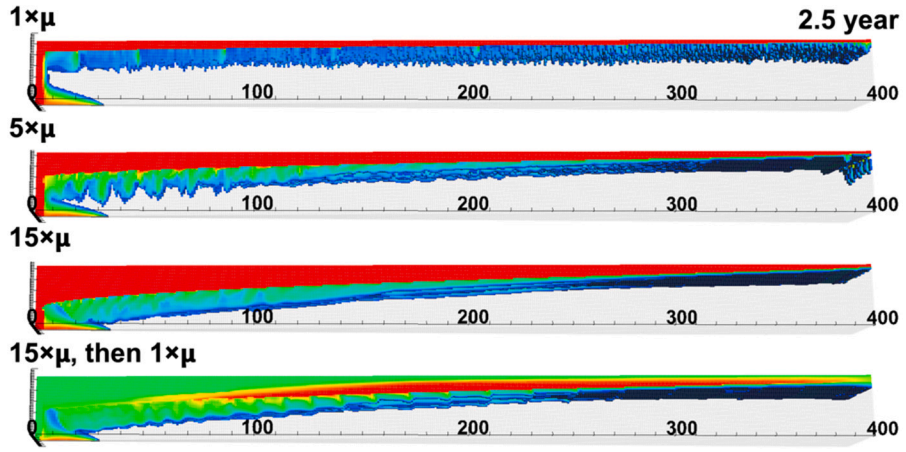

Fig. 5. Case 3: $x_{CO2,w}$ after 2.5 years of injection at 6% PV/yr of neat CO_2, 5× viscosified CO_2, 15× viscosified CO_2, and 15× viscosified CO_2 followed by neat CO_2, for a formation with uniform permeability of $K = 2000$ md.

Finally, we investigate a strategy in which 15× viscosified CO_2 is injected only in the first year followed by neat CO_2 injection to reduce cost.

Figure SI7 shows $x_{CO2,w}$ after one year for neat CO_2, and viscosifications of $5 \times \mu$ and an even higher degree than before, $15 \times \mu$. Fig. 5 presents results after 2.5 years of injection, and also includes the case in which $15 \times \mu$ viscosified CO_2 is injected for one year followed by neat CO_2 injection. Figure SI8 provides the domain-integrated metrics for this case.

4.2. Deep formation

At the temperature and pressure conditions of the relatively shallow formation in the previous example, CO_2 is barely in the supercritical state (starting at 73 bar at the temperature of 323 °K). We repeat simulations from the previous section for a considerably deeper formation with initial temperature and pressure of 373 °K and 241 bar, respectively. At these conditions, the neat CO_2 viscosity is 0.048 cp and the brine viscosity is 0.279 cp, so the viscosity ratio of 5.8 is already improved by a factor 3.7 from the temperature and pressure conditions in the shallower formation. The mass densities are 577 kg/m^3 for CO_2 and 980 kg/m^3 for brine, so the buoyancy force for this smaller density contrast is also reduced. Finally, the CO_2 solubility is 20% higher at 2.4 mole%. Indeed, for all these reasons deeper saline aquifers are generally preferred for CO_2 storage.

Figs. 6 and 7 present results of CO_2 migration for permeabilities of $K = 500$ md (Case 4a) and $K = 2000$ md (Case 4b), respectively, with the corresponding global metric provided in Figures SI9 and SI10.

4.3. Heterogeneous fluvial depositional environment

The detrimental effects of an adverse mobility ratio on fluid displacement are typically more pronounced in heterogeneous formations. If a formation contains fractures or other high permeability conduits for flow, such as layers or depositional channels, low-viscosity CO_2 tend to preferentially flow through such pathways without sweeping much of the tighter regions.

We consider a realistic model for a field-scale CO_2 storage project, specifically the Cranfield site near Natchez, Mississippi. We modeled this project extensively in earlier works by Soltanian et al. (2016a, 2018a,b). Briefly, this is a highly heterogeneous fluvial depositional environment. We adopt a Static Earth Model developed by the Texas Bureau of Economic Geology (Hosseini et al., 2013), which has 8 functional facies with permeabilities ranging from <1 md to ≳700 md and porosities up to 30% (see Figures 3 and 4 in Soltanian et al. (2016a)). We modeled a (tilted) 155 m by 195 m and 24 m Detailed Area of Study (DAS), discretized by $64 \times 51 \times 79$ hexahedral elements. CO_2 was injected from a perforated vertical well located at $x = 97.5$ m, $y = 0$ in three periods of increasing rates.

In this Case 5, we assume continuous injection at the initial rate used at Cranfield, which was 46% PV/year for the DAS. The initial temperature and pressure are 398° K and 320 bar, respectively (comparable to the deep formation conditions in the previous example). At Cranfield, a residual water saturation of $S_{wr} = 40\%$ was assumed with other relative permeability parameters provided in Soltanian et al. (2016a).

We model five scenarios. The first is a reference case with neat CO_2 injection. In the second and third, we assume a 5× and 10× viscosification of CO_2 with all other parameters the same. In the fourth and fifth cases, we assume 5× and 10× viscosification and accompanied by a reduction in residual water to $S_{wr} = 20\%$.

CO_2 flow paths for four of these cases are shown in Fig. 8 as both top- and side-views after injecting 10% PV in 78 days. Dashed red lines highlight the location of the CO_2 fronts in each scenario. The global metrics of CO_2 flow dynamics are given in Figure SI11.

5. Discussion

In the following, we analyze the impact of CO_2 viscosification in more detail through the use of domain-integrated measures that better elucidate the efficiency of the storage process (Figures provided in the Supplemental Information).

5.1. Shallow formation

Case 1: Low permeability of 100 md. Figs. 2, SI4 and SI12 capture the migration characteristics of injected CO_2 for different levels of CO_2 viscosification. Figure SI4 also includes an illustrative reference simulation in which gravity is neglected and CO_2 is viscosified by a factor 10, such that the flow is one-dimensional and viscously stable. Perhaps most intuitively, we find that the plume-tip location and velocity are reduced by CO_2 viscosification. At the time of breakthrough for neat CO_2 (tip location crossing the outflow boundary at 400 m after 2.14 year), the front is only at 245 m for $5 \times \mu$ and 202 m for $10 \times \mu$, i.e. the average tip velocity is reduced about twofold in this period. Tip velocities are not constant, though, and the breakthrough times are 4.8 years for 5× and 6.7 years for 10× viscosified CO_2 (and 11 years in the absence of gravity), which is a factor 2.3 – 3.1 improvement.

The tip location and velocity are derived from a single furthest grid cell with ≥5 mol % CO_2. The COM locations in the vertical z- and radial $R \approx x$ directions, and the corresponding dispersion-widths around those centers, are more accurate metrics that exhibit the same

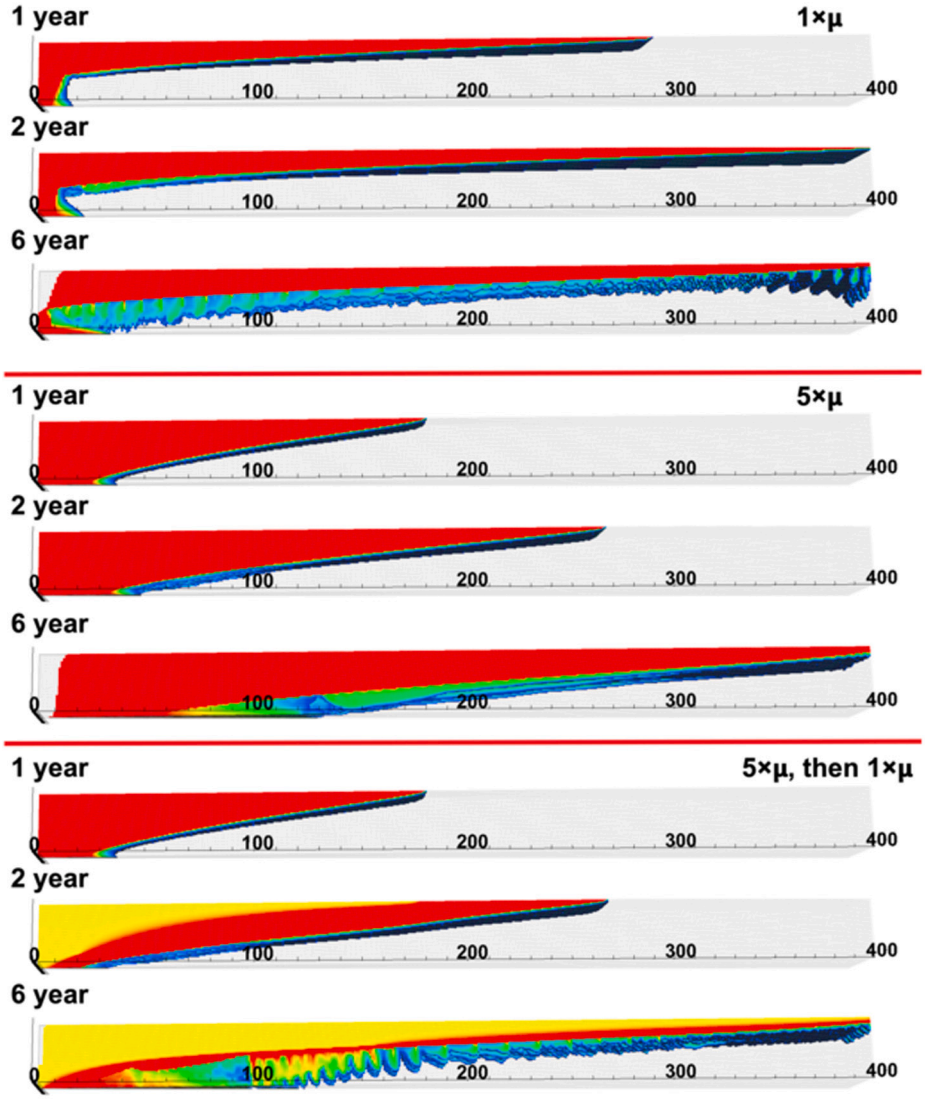

Fig. 6. Case 4a: $x_{CO2,w}$ after 1, 2, and 6 years of injection at 6% PV/yr of neat CO_2, 5× viscosified CO_2, and 5× viscosified CO_2 followed by neat CO_2, for a formation with uniform permeability of $K = 500$ md.

spreading behavior. In the radial direction, we see that around the ~2 year breakthrough time of neat CO_2, the COM (~200 m) and dispersion width (~100 m) are about twice that of the viscosified CO_2. The fact that this is not only due to the viscosity/mobility contrast itself, but also gravity, is clear from the vertical COM and dispersion widths. For the 30-m thickness of the domain, we can see that the COM without gravity would be 15 m. Due to the combination of adverse mobility ratios and buoyancy-driven gravitational override, the COM for neat CO_2 hovers around 25 m with the smallest dispersion width (~4 m). CO_2 viscosification results in a vertically thicker plume, which thus has a ~5 m lower COM with a larger (~7–8 m) dispersion width.

As a measure of storage efficiency, Figure SI12 reports the fraction of injected CO_2 that remains in the modeled domain over time (combined for all simulated cases). We note that this work focusses on the early-time transport within the modeled domain, so most simulations were stopped soon after CO_2 breakthrough at the outflow boundary. Still, the figure shows the enormous impact of retarding the radial spreading of injected CO_2: after around 5 years, all viscosified CO_2 is still stored within the targeted domain, but only 60% of neat CO_2.

One important subtlety to point out is that all the aforementioned measures track *all* CO_2, i.e., both free and dissolved. However, dissolved CO_2 is more desirable than gaseous/supercritical CO_2 which can more easily leak through compromises in the cap rock. When CO_2 spreads faster, this creates a larger CO_2-water interface for CO_2 to dissolve (and also H_2O to evaporate). Indeed, we see in Figure SI4g that the total fraction of dissolved CO_2 is slightly higher for neat CO_2 than for the viscosified cases. This difference is far more pronounced in high-permeability formations, where gravito-convective mixing is more effective, as we will see in other cases below. Here, the solubility trapping is around 10 mole % for all cases.

Figure SI4h demonstrates that all the aforementioned benefits of CO_2 viscosification can be achieved without serious detrimental impacts on injectivity. For neat CO_2 injection, we see the average pressure in the injection well increasing from 90 bar to 95 bar at the onset of injection and then equilibrate back to the initial formation pressure once the CO_2 reaches the outflow boundary (which is kept constant at the initial pressure). The pressure response for the viscosified CO_2 simulations shows similar behavior, but at ~3–6 bar higher pressures.

As an important overall observation: all metrics indicate that the incremental advantages of a $5 \times \mu$ viscosification are far greater than those of another doubling to $10 \times \mu$.

Case 2a: Layers of 1000 md and 100 md. One might assume that for a layered system, CO_2 would primarily channel through the most conductive layers and result in early breakthrough at the outflow boundary.

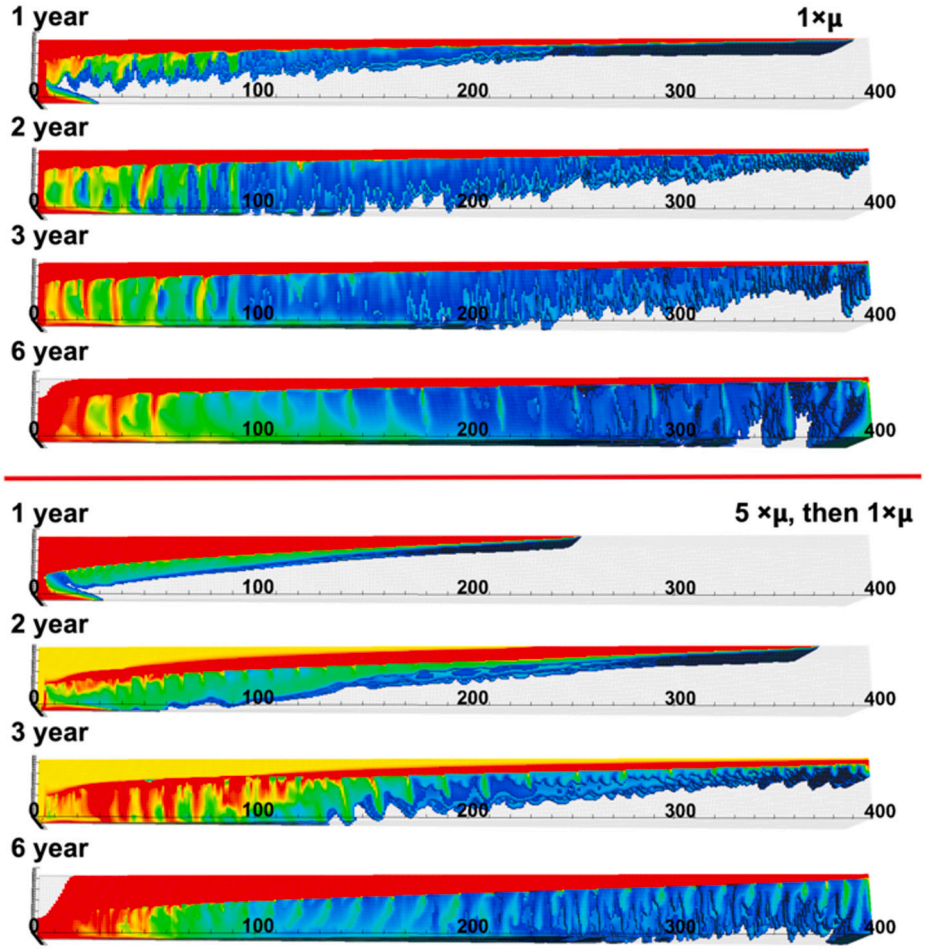

Fig. 7. Case 4b: $x_{CO2,w}$ after 1, 2, 3, and 6 years of injection at 6% PV/yr of neat CO_2 and 5× viscosified CO_2 followed by neat CO_2, for a formation with uniform permeability of $K = 2000$ md.

However, in this case we see in Figs. 3 and SI5 that when the highest-permeability channel is in the bottom, buoyancy is strong enough to still force CO_2 to rise and spread below the cap rock for all levels of viscosification. These more circuitous flow paths actually delay all the breakthrough times, even though both the maximum and average permeabilities are higher than in Case 1.

We can also see in Fig. 3 that considerable gravitational fingering is triggered in the $K = 1000$ md bottom layer. This process mixes dissolved CO_2 throughout the aqueous phase far more effectively than diffusion alone. As a result, we see in Figure SI5g that for neat CO_2 up to nearly 30 mole % of injected CO_2 is subject to solubility trapping at early times versus ~20% and ~15% for $5 \times \mu$ and $10 \times \mu$ viscosified CO_2, respectively. At later times, CO_2 primarily flows through the 100 md top layer which is more gravitationally stable such that the fractional solubility trapping reduces.

Because of the higher average permeability in this case, the differences in pressure response (injectivity) are marginal.

Figure SI12 again illustrates how reduced spreading rates translate into significant impacts on storage efficiencies. Once the neat CO_2 plume reaches the outflow boundary after ~3 years, the fraction of CO_2 that is retained within a 400 m radius decreases steeply (~20%/yr), whereas all injected CO_2 is retained for twice as long (6 years) even for just $5 \times \mu$ viscosification.

Case 2b: Layers of 100 md and 10 md. In this case, the permeabilities of both layers are reduced by a factor ten, which – for a given injection rate – reduces the buoyancy forces relative to advective flow (and increases the pressure response). Indeed, we can see in Fig. 4 and from the vertical dispersion measures in Figure SI6, that flow is confined to the bottom layer for a longer time. Interestingly, though, because the lowest-viscosity neat CO_2 is most susceptible to buoyancy (as well as viscous) forces, it ends up migrating through both the bottom and top layer to a larger degree than for the viscosified CO_2. As a result, overall radial spreading (e.g. COM over time) and breakthrough times are remarkably similar for the different levels of viscosification. At the same time, neat CO_2 again shows a significantly larger degree of solubility trapping (~25% after 3 years).

In this scenario, it appears that the benefits of viscosifying CO_2 might not outweigh the costs. However, in this particular example of the lowest, layered, permeabilities in this study, capillary effects may not be negligible. In a recent experimental study, Ding et al. (2023) injected neat and viscosified CO_2 into a similarly layered core and did not observe significant migration of neat CO_2 into the lower-permeability top layer at that scale.

Case 3: High permeability of 2000 md. For higher permeability formations, the gravitational override is significantly stronger (Figures SI7). Figure SI8 shows nearly an order of magnitude higher tip velocities, higher vertical COM with lower dispersion widths, and earlier breakthrough times. Here, the benefits from viscosifying CO_2, together with a 25% reduction in S_{wr}, can be immense. Breakthrough is delayed from 7.5 months for neat CO_2 to 16 months for $5\times\mu$ and 26 months for $5\times\mu$. As a result, we can see in Figure SI12 that in between the breakthrough times of neat versus viscosified CO_2, the storage efficiency can be 200%–300% higher for the latter.

Fig. 5 presents results after 2.5 years, including the case in which $15 \times \mu$ viscosified CO_2 is injected for one year followed by neat CO_2

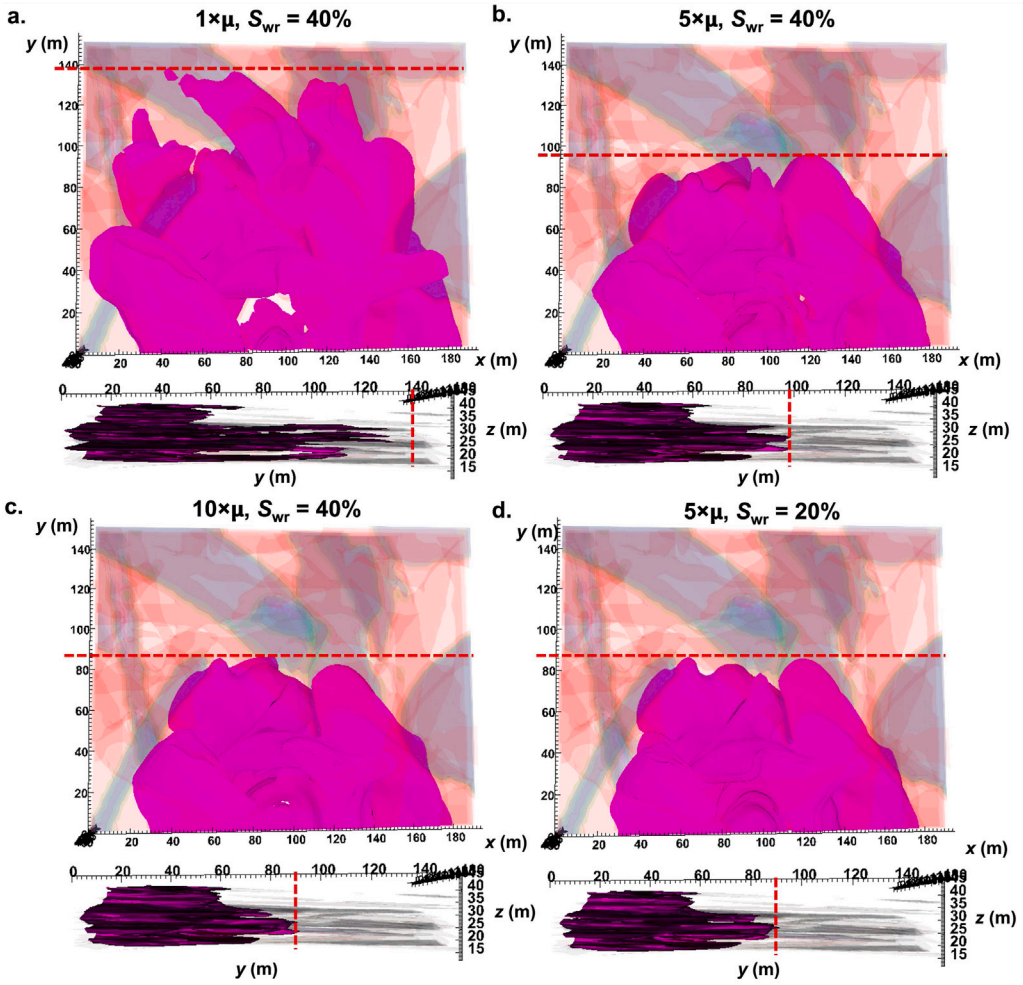

Fig. 8. Case 5: Overall CO_2 molar fraction after 77 days. Blue solid contour is for 10 mole % CO_2, transparent contours illustrate high permeability fluvial conduits for flow. Injection of neat CO_2 (a), 5× viscosified CO_2 (b), and 10× viscosified CO_2 (c) at a residual water saturation of S_{wr} = 40%, and 5× viscosified CO_2 at a reduced residual water saturation of S_{wr} = 20% (d). Each panel shows a top view and a sideview orthogonal to the y-axis. Dashed red lines indicate the location of the CO_2 fronts.

injection. Interestingly, the CO_2 distribution for the latter is quite similar to continuous injection of 15 × μ viscosified CO_2, but at a significantly reduced cost.

Gravitational fingering is pronounced for all viscosities, but mostly for neat CO_2, which develops the largest CO_2-water interface early on. As a result, the solubility trapping efficiency is almost twice as high for neat CO_2 as for viscosified CO_2 (Figure SI8g), so there is a trade-off between maximizing total CO_2 storage efficiency versus optimizing fast solubility trapping.

Injectivity at these high permeabilities is high for all CO_2 viscosities.

5.2. Case 4: Deep formation

The following discussion involves deeper formations for CO_2 storage, which generally are more favorable.

Case 4a: K = 500 md. Because the CO_2-water mobility ratios are more favorable at higher pressures (by a factor 3.7), we see in Figs. 6 and SI9 that the tip location and velocity and other spreading metrics are all quite similar to those in Case 1, even though we consider a fivefold higher permeability here. Again, the results in Fig. 6 suggest that the advantages of injecting viscosified CO_2 can also be achieved by only doing so for a year, followed by neat CO_2 injection.

Unlike in Case 1, we see significant gravitational instabilities develop after a few years and particularly profound for the neat CO_2 case. This contributes again to a significant increase in solubility trapping (Figure SI9g).

In both this and the next case, the injectivity is high and not significantly affected by the viscosification treatment.

Case 4b: K = 2000 md. For a four times higher permeability, the dynamics are quite different due to profound gravitational instabilities, as shown in Fig. 7. The spreading rates and breakthrough times are clearly accelerated (Figure SI10). As before, we see that the retardation of the CO_2 front by viscosification increases the overall retention of CO_2 in the domain (Figure SI12), but also that neat CO_2 creates a large surface area of CO_2 dissolution and mixing, which results in about double the degree of solubility trapping.

Finally, we see a thermodynamic phenomenon that is not captured in many reservoir simulators: because our EOS-based phase-split computations self-consistently allow all species to transfer between all phases, CO_2 not only dissolves into water, but H_2O also evaporates into the CO_2-rich phase. This evaporation allows the water saturation to drop below the residual saturation. Eventually all water evaporates in the near-well region, which is why in Fig. 7 we see no water-dissolved CO_2 near the well after 6 years.

5.3. Case 5: Heterogeneous fluvial depositional environment

CO_2 flow paths are more complicated in highly heterogeneous formations, such as the fluvial depositional setting in the Cranfield

large-volume CO_2 storage pilot project. Fig. 8 illustrates that, as expected, for neat CO_2 injection the flow paths are strongly dominated by the fluvial channels and are already close to escaping the Detailed Area of Study after 77 days, or 10% PVI. This is of concern not just because of the poor sweep in general, as in the previous examples, but also because the exact locations of specific subsurface preferential flow conduits are generally unknown and CO_2 may migrate out of the zones leased for a storage project.

Viscosifying the CO_2 delays the migration front and results in more radial, and thus more predictable, flow. After 77 days, the neat CO_2 front is at 138 m, the $5\times\mu$ CO_2 is at 95 m, and the $10\times\mu$ CO_2 at 86 m, which corresponds to an average 38% slower tip velocity. Interestingly, the simulation with $5\times\mu$ as well as a S_{wr} reduction from 40% to 20% has the exact same front location as the $10\times\mu$ simulation without that reduction in S_{wr} (metrics for $10\times\mu$ with S_{wr} reduction are included in Figure SI11). This is obviously attractive because a fivefold viscosity reduction is easier to achieve than $10\times\mu$, but also – and perhaps more importantly – because we see in Figure SI11b that the pressure build-up for $10\times\mu$ CO_2 may be unacceptably high (76 bar higher than for neat CO_2), whereas $5\times\mu$ results in less than half that pressure increase (35 bar) for the same sweep efficiency.

Figure SI12 again illustrates the impact of delayed breakthrough times on the fraction of injected CO_2 that is retained within the modeled domain, shown for an extended 1-year time period.

We note that for the duration of the simulations presented here, the water saturations throughout most of the domain remain well above S_{wr}, so the beneficial impact of reducing S_{wr} will become even more pronounced at later times, when a reduction in residual water proportionally increases the available storage capacity for CO_2.

Finally, the degree of solubility trapping for neat CO_2 is again significantly higher than for viscosified CO_2 (Figure SI11a), in this case by a factor two relative to the $5\times\mu, S_{wr}=20\%$ and $40\times\mu, S_{wr}=40\%$ scenarios.

6. Conclusions

The main findings from our large-scale simulations of viscosified CO_2 injection in subsurface aquifers are:

1. As expected, in most cases a fivefold viscosification of CO_2, as achieved experimentally by Kar et al. (2022), significantly delays the spreading of injected CO_2, improving the sweep and storage efficiency in a given target domain.
2. The impact of CO_2 viscosification on migration pathways is highly non-linear, especially in heterogeneous formations, and we find that for all cases investigated the benefits from a fivefold viscosifications are far greater than the incremental improvements of a tenfold viscosity reduction.
3. Kar et al. (2022) also found that their functional molecule selected for viscosification reduces residual water saturations by about 30%. Such a reduction in S_{wr} further delays the CO_2 spreading, increases the accessible storage pore volume, and – importantly – alleviates detrimental impacts on injectivity due to the higher CO_2 viscosity.
4. While viscosifying CO_2 increases the *total* amount of CO_2 that can be stored in a given volume and amount of time, the amount of *dissolved* CO_2 is significantly higher for neat CO_2. In other terms, viscosified CO_2 benefits structural trapping while neat CO_2 promotes solubility trapping. Neat CO_2 also offers the highest injectivity. This means that there may be both scenarios where CO_2 viscosity is highly advantageous (e.g. in confining CO_2 laterally within leased areas and/or away from distant abandoned wells or other compromises in the cap rock such as fractures), but there may also be conditions where the extent of the CO_2 plume is of less concern and the high injectivity and longer-term solubility trapping of neat CO_2 are more desirable.
5. Direct CO_2 viscosification avoids some of the injectivity challenges associated with CO_2-foam, because there is no (incompressible) water co-injected. Moreover, if the direct viscosification treatment is accompanied by a reduction in residual water saturation, as observed in experiments (and also for CO_2-foam), this effectively creates more storage pore volume for CO_2 and further improves injectivity.
6. Preliminary simulations suggest that there may be no need for *continued* injection of viscosified CO_2. We find virtually no difference between injecting viscosified CO_2 continuously for, say, 5 years versus injecting the viscosified CO_2 only in the first year followed by neat CO_2 injection. This approach warrants further investigation in a future work.

In one of our modeled scenarios (Case 2b), neat CO_2 exhibits more buoyancy-driven cross-flow between layers of different permeabilities than viscosified CO_2 and the more efficient solubility trapping for neat CO_2 appears to perhaps outweigh the benefits of CO_2 viscosification. However, our assumption of negligible capillary effects may break down for such systems of 10 md–100 md layers (Ding et al., 2023). The impacts of capillarity on viscosified CO_2 injection, where relevant, is another subject for future analyses.

CRediT authorship contribution statement

Joachim Moortgat: Methodology, Software, Formal analysis, Investigation, Resources, Data curation, Writing – original draft, Writing – review & editing, Visualization. **Abbas Firoozabadi:** Conceptualization, Methodology, Writing – original draft.

Declaration of competing interest

The authors declare that they have no known competing financial interests or personal relationships that could have appeared to influence the work reported in this paper.

Data availability

No data was used for the research described in the article.

Appendix A. Supplementary data

Supplementary material related to this article can be found online at https://doi.org/10.1016/j.ijggc.2023.103984.

References

Adebayo, A.R., 2018. Viability of foam to enhance capillary trapping of co2 in saline aquifers—an experimental investigation. Int. J. Greenh. Gas Control 78, 117–124.
Afra, S., Alhosani, M., Firoozabadi, A., 2023. Improvement in co2 geo-sequestration in saline aquifers by viscosification: From molecular scale to core scale. Int. J. Greenh. Gas Control 125, 103888.
Amooie, M.A., Soltanian, M.R., Moortgat, J., 2017. Hydrothermodynamic mixing of fluids across phases in porous media. Geophys. Res. Lett. 44, 3624–3634.
Amooie, M.A., Soltanian, M.R., Moortgat, J., 2018. Solutal convection in porous media: Comparison between boundary conditions of constant concentration and constant flux. Phys. Rev. E 98, 033118.
Ding, B., Kantzas, A., Firoozabadi, A., 2023. Real-time 3d imaging of neat, and viscosified co2 in displacement of brine-saturated porous media. In: SPE Annual Technical Conference and Exhibition. SPE, SPE–214842.
Firoozabadi, A., Myint, P.C., 2010. Prospects for subsurface co2 sequestration. Aiche J. 56, 1398–1405.
Føyen, T., Brattekås, B., Fernø, M., Barrabino, A., Holt, T., 2020. Increased co2 storage capacity using co2-foam. Int. J. Greenh. Gas Control 96, 103016.
Hirasaki, G.J., Lawson, J., 1985. Mechanisms of foam flow in porous media: apparent viscosity in smooth capillaries. Soc. Pet. Eng. J. 25, 176–190.
Hosseini, S.A., Lashgari, H., Choi, J.W., Nicot, J.P., Lu, J., Hovorka, S.D., 2013. Static and dynamic reservoir modeling for geological co2 sequestration at cranfield, mississippi, usa. Int. J. Greenh. Gas Control 18, 449–462.
Hoteit, H., Firoozabadi, A., 2009. Numerical modeling of diffusion in fractured media for gas-injection and-recycling schemes. Spe J. 14, 323–337.

Hovorka, S.D., Meckel, T.A., Trevino, R.H., Lu, J., Nicot, J.P., Choi, J.W., Freeman, D., Cook, P., Daley, T.M., Ajo-Franklin, J.B., et al., 2011. Monitoring a large volume co2 injection: Year two results from secarb project at denbury's cranfield, mississippi, usa. Energy Procedia 4, 3478–3485.

Ide, S.T., Jessen, K., Orr, Jr., F.M., 2007. Storage of co2 in saline aquifers: Effects of gravity, viscous, and capillary forces on amount and timing of trapping. Int. J. Greenh. Gas Control 1, 481–491.

Izadi, M., Kam, S., 2020. Investigating supercritical co2 foam propagation distance: conversion from strong foam to weak foam vs. gravity segregation. Transp. Porous Media 131, 223–250.

Kar, T., Cho, H., Firoozabadi, A., 2022. Assessment of low salinity waterflooding in carbonate cores: Interfacial viscoelasticity and tuning process efficiency by use of non-ionic surfactant. J. Colloid Interface Sci. 607, 125–133.

Kar, T., Firoozabadi, A., 2022. Effective viscosification of supercritical carbon dioxide by oligomers of 1-decene. Iscience 25, 104266.

Li, Z., Firoozabadi, A., 2009. Cubic-plus-association equation of state for water-containing mixtures: Is cross association necessary? Aiche J. 55, 1803–1813.

Lyu, X., Voskov, D., Rossen, W.R., 2021. Numerical investigations of foam-assisted co2 storage in saline aquifers. Int. J. Greenh. Gas Control 108, 103314.

Moortgat, J., 2017. Adaptive implicit finite element methods for multicomponent compressible flow in heterogeneous and fractured porous media. Water Resour. Res. 53, 73–92.

Moortgat, J., 2018. Reservoir simulation with the cubic plus (cross-) association equation of state for water, co2, hydrocarbons, and tracers. Adv. Water Resour. 114, 29–44.

Moortgat, J., Amooie, M.A., Soltanian, M.R., 2016. Implicit finite volume and discontinuous galerkin methods for multicomponent flow in unstructured 3d fractured porous media. Adv. Water Resour. 96, 389–404.

Moortgat, J., Firoozabadi, A., 2013a. Fickian diffusion in discrete-fractured media from chemical potential gradients and comparison to experiment. Energy Fuels 27, 5793–5805.

Moortgat, J., Firoozabadi, A., 2013b. Higher-order compositional modeling of three-phase flow in 3d fractured porous media based on cross-flow equilibrium. J. Comput. Phys. 250, 425–445.

Moortgat, J., Firoozabadi, A., 2013c. Three-phase compositional modeling with capillarity in heterogeneous and fractured media. SPE J. 18, 1150–1168.

Moortgat, J., Firoozabadi, A., 2016. Mixed-hybrid and vertex-discontinuous-galerkin finite element modeling of multiphase compositional flow on 3d unstructured grids. J. Comput. Phys. 315, 476–500.

Moortgat, J., Firoozabadi, A., 2017. Water coning, water, and co2 injection in heavy-oil fractured reservoirs. SPE Reserv. Eval. Eng. 20, 168–183.

Moortgat, J., Firoozabadi, A., Li, Z., Espósito, R., 2010. Experimental coreflooding and numerical modeling of co2 injection with gravity and diffusion effects. In: SPE Annual Technical Conference and Exhibition?. SPE, SPE–135563.

Moortgat, J., Firoozabadi, A., Li, Z., Esposito, R., 2013. Co2 injection in vertical and horizontal cores: measurements and numerical simulation. Spe J. 18, 331–344.

Moortgat, J., Li, Z., Firoozabadi, A., 2011. Three-phase compositional modeling of co2 injection by higher-order finite element methods with cpa equation of state. In: SPE Reservoir Simulation Symposium. OnePetro.

Moortgat, J., Schwartz, F.W., Darrah, T.H., 2018. Numerical modeling of methane leakage from a faulty natural gas well into fractured tight formations. Groundwater 56, 163–175.

Nasrabadi, H., Moortgat, J., Firoozabadi, A., 2016. New three-phase multicomponent compositional model for asphaltene precipitation during co2 injection using cpa-eos. Energy Fuels 30, 3306–3319.

Peng, D.Y., Robinson, D.B., 1976. A new two-constant equation of state. Ind. Eng. Chem. Fundam. 15, 59–64. http://dx.doi.org/10.1021/i160057a011.

Rossen, W.R., Farajzadeh, R., Hirasaki, G.J., Amirmoshiri, M., 2022. Potential and challenges of foam-assisted co2 sequestration. In: SPE Improved Oil Recovery Conference. OnePetro.

Rossen, W., Zeilinger, S., Shi, J.X., Lim, M., 1999. Simplified mechanistic simulation of foam processes in porous media. SPE J. 4, 279–287.

Soltanian, M.R., Amooie, M.A., Cole, D.R., Darrah, T.H., Graham, D.E., Pfiffner, S.M., Phelps, T.J., Moortgat, J., 2018b. Impacts of methane on carbon dioxide storage in brine formations. Groundwater 56, 176–186.

Soltanian, M.R., Amooie, M.A., Cole, D.R., Graham, D.E., Hosseini, S.A., Hovorka, S., Pfiffner, S.M., Phelps, T.J., Moortgat, J., 2016a. Simulating the cranfield geological carbon sequestration project with high-resolution static models and an accurate equation of state. Int. J. Greenh. Gas Control 54, 282–296.

Soltanian, M.R., Amooie, M.A., Cole, D., Graham, D., Pfiffner, S., Phelps, T., Moortgat, J., 2018a. Transport of perfluorocarbon tracers in the cranfield geological carbon sequestration project. Greenh. Gases: Sci. Technol. 8, 650–671.

Soltanian, M.R., Amooie, M.A., Dai, Z., Cole, D., Moortgat, J., 2016b. Critical dynamics of gravito-convective mixing in geological carbon sequestration. Sci. Rep. 6 (35921).

Vitoonkijvanich, S., AlSofi, A.M., Blunt, M.J., 2015. Design of foam-assisted carbon dioxide storage in a north sea aquifer using streamline-based simulation. Int. J. Greenh. Gas Control 33, 113–121.